

UNCLASSIFIED

DETERMINING THE AEROTHERMODYNAMIC ENVIRONMENT OF A GENERIC MISSILE

BY

Matthew E. Zuber*, Matthew C. Towne**, Alice J. Chen**, John J. Bertin***, and Robert J. Butler**
Department of Aeronautics, The U. S. Air Force Academy

Abstract

There are a variety of computer codes of varying degrees of rigor which can be used by the designers of high-speed missile systems in order to define the aerothermodynamic environment at flight conditions. It is assumed that the flow models and the numerical algorithms used in these codes have been validated by their developers. However, the users of such codes must exercise them against a quality data base, gaining knowledge of the intricacies in the use of such codes and calibrating the range of conditions over which the code can be used to predict specific parameters that are important to the design objectives without necessarily verifying that all the features of the flow are correctly modeled. Data which can be used to define the aerothermodynamic environment of a generic missile have been obtained in the Tri-Sonic Wind Tunnel (TWT) of the Aeronautical Research Center (ARC) at the U. S. Air Force Academy (USAF). Forces and moments, surface pressures, surface temperatures, and flow visualization photographs have been obtained at a Mach number of 4.28 over a range of Reynolds numbers (based on the free-stream conditions and model length) from 1×10^7 to 1.5×10^7 . The experimentally-determined parameters are compared in the present paper with parameters computed using the Reynolds-Averaged Navier-Stokes equations in the GASP v3 code and with the aerodynamic coefficients computed using the ATAP code.

*Captain, USAF, Student Member of AIAA

**Major, USAF, Senior Member of AIAA

***Professor of Aeronautics, Fellow of AIAA

Financial support for this effort was provided by the Wright Laboratory/Armament Directorate/Munitions Seeker and Evaluation Branch (WL/FMGI) at the Eglin Air Force Base through Project Order QFY76219725005.

This paper is declared a work of the U. S. Government and is not subject to copyright protection in the United States.

Nomenclature

| | |
|-------------------------|--|
| A_x | Axial Force |
| C_A | Axial-force coefficients ($A_x/q_\infty S$) |
| C_N | Normal-force coefficients ($N/q_\infty S$) |
| C_M | Pitching moment coefficients referenced to the apex of the model ($M/q_\infty S D$) |
| D | Diameter of the cylindrical portion of the model, 1.25 inches (3.18 cm.) |
| M | Pitching moment referenced to the apex of the model |
| p | Static pressure |
| p_{t1} | Total pressure in the tunnel reservoir |
| L | Model length, 10.00 inches (25.40 cm.) |
| N | Normal Force |
| r | Recovery factor |
| $Re_{\infty,L}$ | Reynolds number based on the free-stream conditions and on the model length |
| Re_L | Reynolds number based upon the free stream conditions and on the model length in millions (i.e., $Re_L = Re_{\infty,L} \times 10^{-6}$) |
| S | Reference area ($\pi D^2/4$) |
| s | Wetted distance measured from the apex of the model |
| T_{recovery} | Recovery temperature, see eq. (4) |
| T_{t1} | Total temperature in the tunnel reservoir |
| V | Velocity |
| x_{cp}/L | Distance measure along the model axis, measured from the apex of the model |
| α | Angle of attack |
| ϵ, η, ζ | Coordinate system for the GASP v3 computations (axial, semi-circumferential, and normal) |
| ϕ | Angle measured relative to the leeward plane of symmetry |
| μ | Viscosity |
| ρ | Density |
| Subscripts | |
| $t1$ | Conditions in the reservoir (or stilling chamber) of the wind tunnel |
| 1 or ∞ | Free-stream conditions |
| eff | Effective angle of attack, sum of specified and offset angles of attack, see eq. (2) |

19970912 099

Introduction

The designers of high-speed missile systems make extensive use of computer codes in order to define the aerothermodynamic environment at flight conditions. Reliance on computational fluid dynamic (CFD) codes for predicting the flight environment is due in part to the inability of ground-test facilities to provide a complete match of all the pertinent simulation parameters for the flowfields and in part to rapid advances in computer hardware and software. There are many sophisticated codes which apply the Navier Stokes equations (in varying degrees of rigor) to the entire flowfield. Some codes are used primarily by the organization responsible for their development, e. g., the Langley Aerothermodynamic Upwind Relaxation Algorithm (LAURA) code¹. Other codes, which have been widely distributed, are used by organizations throughout the world, e. g., the General Aerodynamic Simulation Program version 3 (GASP v3) code². The developers of such computational codes must first determine what fluid-dynamic phenomena are important to the expected applications of the code. Numerical models of suitable rigor must be developed for the important fluid-dynamic phenomena. Once the numerical models have been developed, the code developers must validate them and determine the range of conditions over which the models are applicable. Bradley³ defines the concept of code validation as follows. "CFD code validation implies the comparison of detailed surface and flowfield parameters with the corresponding experimental values to verify the code's ability to model accurately the critical physics of the flow. Validation can occur only when the accuracy and limitations of the experimental data are known and thoroughly understood and when the accuracy and limitations of the code's numerical algorithms, grid density effects, and physical basis are equally known and understood over a range of specified parameters." Mehta⁴ states: "Validation is defined as the process of assessing the credibility of the simulation model, within its domain of applicability, by determining whether the right simulation model is developed and by estimating the degree to which this model is an accurate representation of reality from the perspective of its intended uses."

Bradley³ defines the concept of code calibration as follows. "CFD code calibration implies the comparison of CFD code results with experimental data for realistic geometries that are similar to the ones of design interest, made in order to provide a measure of the code's ability to predict specific parameters that are

important to the design objectives without necessarily verifying that all the features of the flow are correctly modeled." Furthermore, Bradley⁵ has said: "Engineers have always been able to use less than perfect tools coupled with experiences and calibration to known physical quantities to provide design guidance. Calibration and validation should not be confused. Calibration provides an error band or correction factor to enhance the ability of a particular code to predict specific parameters that are important to the design objectives for a particular design without verifying that all other features of the flow are modeled accurately. For example, one might calibrate a code's ability to predict shock location and lift and moment on a wing without any assurances that the flowfield off the surface and the wake behind the wing are properly modeled. Or one may calibrate a code's ability to compute the gross pressure loss through a supersonic inlet-duct combination without concern for the distortion distribution at the compressor face. Although the use of calibrated CFD solutions is dangerous because of the subtle viscous interactions that are extremely sensitive to geometry and flowfield, skilled engineers can often obtain useful design information and guidance from relatively immature codes."

There are a variety of codes which employ relatively simple analytical models, empirical correlations, and two-layer flowfield models (Euler equations to model the inviscid flow coupled with a boundary-layer formulation). As noted by Martellucci⁶, "These approximate techniques are very efficient, typically requiring only seconds on small computers, and are 'robust' in the sense of almost always producing a solution." Several organizations have developed a family of design codes that provide engineering level or preliminary-design estimates of aerodynamic forces and moments acting on missiles of arbitrary shapes flying at supersonic/hypersonic speeds. These design codes include M3HAX⁷, NSWC AP95⁸, and Missile DATCOM⁹. As discussed in Refs. 7, 8, and 9, which were presented in a session dedicated to approximate techniques, these codes are continually being modified to improve the existing models for flow phenomena and to add subroutines that can address new problems. Another code which employs approximate techniques is the Aerothermal Target Analysis Program (ATAP) code¹⁰.

Data which can be used to define the aerothermodynamic environment of a generic missile have been obtained in the Tri-Sonic Wind Tunnel (TWT) of the Aeronautical Research Center (ARC) at

the U. S. Air Force Academy (USAFA). Forces and moments, surface pressures, surface temperatures, and flow visualization photographs have been obtained at a Mach number of 4.28 over a range of Reynolds numbers (based on the free-stream conditions and on the model length) from 1×10^7 to 1.5×10^7 . The experimentally-determined parameters are compared in the present paper with parameters computed using the Reynolds-Averaged Navier-Stokes equations in the GASP v3 code and with the aerodynamic coefficients computed using the ATAP code. The objectives of the comparisons include (1) the verification of the quality of the data from the TWT and (2) the continuation of the effort to calibrate the computational tools available to the ARC/Department of Aeronautics for teaching and for research. Once the quality of the experimental measurements has been verified, the data can be used to improve the models used in the ATAP code.

Experimental Program

Facility

The experimental investigation utilized the Tri-Sonic Wind Tunnel (TWT), which is a blow-down facility that discharges to the atmosphere, as shown in Fig. 1. The compressed air for the wind tunnel is generated by a pair of rotary screw-type compressors. From the compressors, the air is routed through a pair of drying towers and stored in six holding tanks. The dewpoint of the dried air is -50°F (-45°C), when the tank temperature of 100°F (38°C) and the tank pressure is 600 psia ($4.137 \times 10^6 \text{ N/m}^2$). As a result, the absolute humidity of the dried air is less than $2 \times 10^{-6} \text{ kg H}_2\text{O}$ per kg dry air. For a run, the air passes from the holding tanks, through a series of control valves, into a stilling chamber, through a convergent/divergent nozzle, and into the 1-foot (0.3048 m) by 1-foot (0.3048 m) test section. The total pressure in the stilling chamber is sensed by a transducer with a full-scale range of 300 psia ($2.068 \times 10^6 \text{ N/m}^2$) with a combined nonlinearity and hysteresis of $\pm 0.3\%$ full scale. The maximum total pressure in the stilling chamber, which occurs at the higher Mach numbers (see Fig. 2) is 250 psia ($1.724 \times 10^6 \text{ N/m}^2$). The total temperature in the stilling chamber is sensed by a Type E (chromel/constantan) thermocouple capable of measuring -328°F to 1652°F (-200°C to 900°C) with a sensitivity of $67.9 \text{ microvolts}/^\circ\text{C}$. The total temperature varies only slightly, being 560°R (311K) $\pm 20^\circ\text{R}$ ($\pm 11\text{K}$).

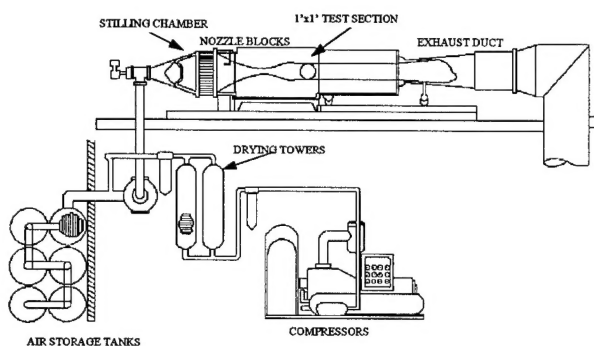


Figure 1: Schematic of USAF Academy Tri-Sonic Wind Tunnel

Fixed nozzle blocks form the convergent/divergent nozzle through which the air accelerates from the stilling chamber into the test section. Nozzle blocks are available to provide test section Mach numbers at specific, selected design values in the range of 0.14 to 4.50. To avoid choking the test section flows at transonic Mach numbers (less than one), a porosity cart is usually used. As shown in Fig. 2, the operating range of total pressure in the tunnel reservoir (p_{t1}) is a function of the test-section Mach number. By varying the pressure in the stagnation chamber of the TWT, one can control the unit free-stream Reynolds number in the test section. It is possible to generate free-stream unit Reynolds numbers from approximately 6×10^6 per foot (2×10^7 per meter) to approximately 36×10^6 per foot (12×10^7 per meter). The range of test conditions possible in this facility are indicated in Fig. 2.

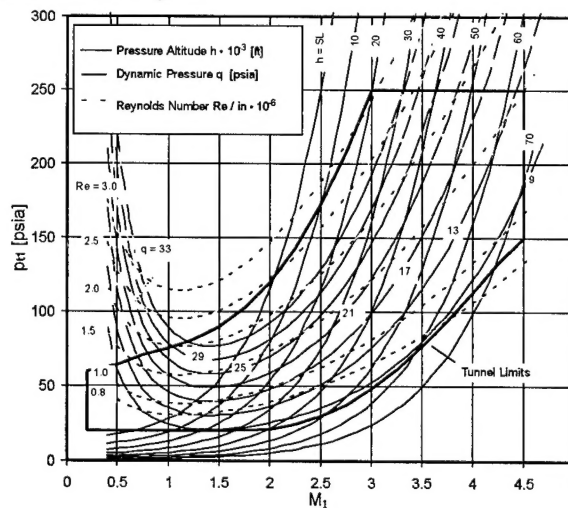


Figure 2: Tri-Sonic Wind Tunnel performance capabilities

The run time is a function of the total temperature (T_{t1}), the total pressure in the tunnel reservoir (p_{t1}), and the nozzle throat area (which, since the cross-section area of the test section is fixed, relates uniquely to the Mach number in the test section). Usable run times range from 20 seconds to 420 seconds.

Instrumentation

The static pressures acting on the model surface at the locations identified in Table 1 were transmitted through a pressure orifice formed by stainless steel tubing, which had an inside diameter of 0.0310 in. (0.0787 cm.) and was mounted flush to the model surface. The pressures then passed through approximately ten feet (305 cm.) of tygon tubing, which had an inside diameter of 0.0313 in. (0.0794 cm.) and an outside diameter of 0.0938 in. (0.238 cm.), to a scani-valve which housed the pressure transducer. For the present tests, a kulite differential-pressure transducer with a full-scale range of 15 psid (1.03×10^5 N/m², differential) and a combined nonlinearity and hysteresis of $\pm 0.5\%$ full scale was used to measure the gage pressure relative to the static pressure in the ARC. The reference (atmospheric) pressure was measured by a Heise digital pressure indicator with a full-scale range of 17.19 psia (1.185×10^5 N/m²). Including the effects of sensitivity, hysteresis, nonlinearity, and repeatability, the atmospheric pressure measurement had an uncertainty of $\pm 0.035\%$ of the full-scale measurement at 70°F (21°C).

Table 1 Locations of pressure orifices

| Orifice Number | x/L | ϕ (degrees) |
|----------------|--------|---------------------|
| 1 | 0.7754 | 0 |
| 2 | 0.6600 | 180 |
| 3 | 0.5721 | 0 |
| 4 | 0.4720 | 180 |
| 5 | 0.3722 | 0 |
| 6 | 0.3468 | 0 |
| 7 | 0.3385 | 180 |
| 8 | 0.3385 | 0 |
| 9 | 0.2817 | 180 |
| 10 | 0.2273 | 0 |
| 11 | 0.1722 | 180 |
| 12 | 0.1160 | 0 |
| 13 | 0.0600 | 180 |
| 14 | 0.0430 | 0 |
| 15 | 0.0000 | 0 |

Because of the long length of tygon tubing connecting the pressure orifice in the model to the

scani-valve/transducer, all pressure measurements were time-averaged, "steady-state" values. Once the flow was established, there was a 3000 ms delay before the first pin of the scani-valve was recorded. There was a 200 ms delay between each of the subsequent steps.

A six component force and moment balance was used to sense the forces and the moments acting on the models. The balance provided measurements that could be used to determine the axial force, the side force, the normal force, the pitching moment, the rolling moment, and the yawing moment. The capability and the accuracy of the individual components of the six-component balance were:

N1: 100 lbf (445 N) $\pm 0.25\%$ full scale
 N2: 100 lbf (445 N) $\pm 0.25\%$ full scale
 Y1: 50 lbf (222 N) $\pm 0.25\%$ full scale
 Y2: 50 lbf (222 N) $\pm 0.25\%$ full scale
 Axial: 25 lbf (111 N) $\pm 0.25\%$ full scale
 Rolling moment: 60 in lbf (6.8 N m) $\pm 0.25\%$ full scale

Therefore, the uncertainty of a given axial-force measurement was ± 0.0625 lbf (± 0.278 N). Since typical measured values of the axial force were in the range 5 lbf to 10 lbf (22 N to 44 N), the corresponding uncertainties (given as a percent of that measured value) are: + 1.25% to 0.63%, respectively. When the model was at an angle of attack of $\pm 10^\circ$, typical maximum values of the normal force were 28 lbf (125 N). Thus, the corresponding uncertainty is 0.2% of this measured value for the normal force.

Liquid crystals (LCs) were also used to provide information about the flowfield for the generic missile configuration. LCs are substances which in certain phases have the mechanical properties of a liquid but the optical properties of a crystal. Two types of liquid crystals are shear sensitive or thermochromic (temperature) sensitive. Thermochromic liquid crystals (TLCs) were used in the present experimental program, specifically, a Hallcrest 12C1W TLC with a 0.9°F (0.5°C) bandwidth and a color play starting at 55.3°F (13.3°C) and ending at 54.4°F (12.8°C). (The calibration of this TLC to verify the manufacturer's temperature is underway, but has not been completed.) By using a TLC with a specific, narrow color-play band, one can record the times and the surface areas, when the model surface passes through this temperature range. With this information, one can quickly obtain qualitative information about the flow (identify hot spots, the onset of boundary-layer transition, and

regions where the flow has separated from the surface) or determine the magnitude of the local heat transfer. Several studies have been accomplished using LCs to quantify the aerothermodynamic environment of models exposed to high-speed flows^{11,12}.

To optimize the information obtained using TLCs, the model must be constructed of a material with the proper thermal conductivity, density, and specific heat. Thus, the model for the present tests was constructed of ertalyteTM. The test surface was first air brushed with black paint and then with a coating of the TLC. A Sony XC-003 RGB camera and a Matrox Meteor RGB frame grabber captured the image files. A time code generator was also used to measure time to a precision of 0.01 seconds and be placed upon the images grabbed. A Micron 166 MHz PC with 128 MB of RAM stored the images until transfer to the hard drive was completed. Images were stored in a TIFF 6.0 format in 24 bit color RGB with a resolution of 640x480. Imaging95 was used to convert the TIFF 6.0 images to TIFF 5.0.

Test Conditions

The free-stream Mach number in the test section was 4.28 ± 0.04 . This is the average value determined from a facility calibration program in which an eleven probe pitot rake was rotated in 30° increments. These pitot-pressure measurements were used to generate Mach number contours for three planes in the test section: one at the upstream end, a second in the middle, and the third at the downstream end of the test section. This value has been verified in repeated investigations of the flow quality of the TWT. Force-and-moment data were obtained at three nominal values of the total pressure in the tunnel reservoir. Specifically, $p_{t1} = 150$ psia (1.034×10^6 N/m²), 200 psia (1.379×10^6 N/m²), and 225 psia (1.551×10^6 N/m²). Pressure measurements were obtained at a single (nominal) value of $p_{t1} = 200$ psia (1.379×10^6 N/m²). There was a single (nominal) total temperature for all of the runs, $T_{t1} = 560$ °R (311K).

The perfect-gas relations were used to calculate the free-stream conditions, assuming that the flow accelerated isentropically from the nominal stagnation conditions to the Mach 4.28 free stream. Sutherland's equation¹³ was used to calculate the free-stream viscosity. When $p_{t1} = 200$ psia (1.379×10^6 N/m²), the free-stream unit Reynolds number is:

$$Re_{\infty/L} = \rho_1 V_1 / \mu_1 = 16.3 \times 10^6 \text{ per foot} =$$

$$53.5 \times 10^6 \text{ per meter}$$

The free-stream Reynolds number based on the length of the model is 13.6×10^6 . However, as noted in Ref. 13, "one would expect that the actual viscosity is 3 percent to 5 percent greater than Sutherland's value" at the temperatures characteristic of the free-stream flow in a supersonic/hypersonic wind tunnel.

In this report, we will sometimes use ReL as the shorthand notation for the Reynolds number based on the free-stream conditions and the model length.

$$Re_{\infty L} = \rho_1 V_1 L / \mu_1 = ReL \times 10^6 \quad (1)$$

Since the free-stream Mach number and the total temperature were essentially the same for all runs, the Reynolds number and the dynamic pressure were directly proportional to the total pressure. Thus, for a nominal value of $p_{t1} = 150$ psia (1.034×10^6 N/m²), ReL was approximately 9.95; for a nominal value of $p_{t1} = 200$ psia (1.379×10^6 N/m²), ReL was approximately 13.6; and for a nominal value of $p_{t1} = 225$ psia (1.551×10^6 N/m²), ReL was approximately 15.2.

Model

A two-view, dimensioned sketch of the generic missile wind-tunnel configuration is presented in Fig. 3. The overall length of the wind-tunnel configuration (L) is 10.00 in. (25.40 cm.). The L/D ratio (where D is the diameter of the cylindrical portion of the missile) is 8.00. There were actually two wind-tunnel models built for these wind-tunnel tests. The first model, which was built for the force-and-moment tests, was constructed in two parts: a forebody made of aluminum and an afterbody of brass for the fins. Once the force-and-moment phase of the test program had been completed, the model was modified with 15 orifices to provide information about the surface pressure distribution. The second model was constructed from one piece of ertalyteTM. This material has thermal properties appropriate for the use of liquid crystals to determine the heat transfer.

There were slight differences in the dimensions of the two models. The two models had a small nose radius: 0.056 in. (0.142 cm.) for the heat-transfer model and 0.064 in. (0.163 cm.) for the pressure model. The conical half angles were 9.0° and 9.4° for the heat-transfer and for the pressure models, respectively. The cylindrical section started at 3.691 in. (9.375 cm.) from

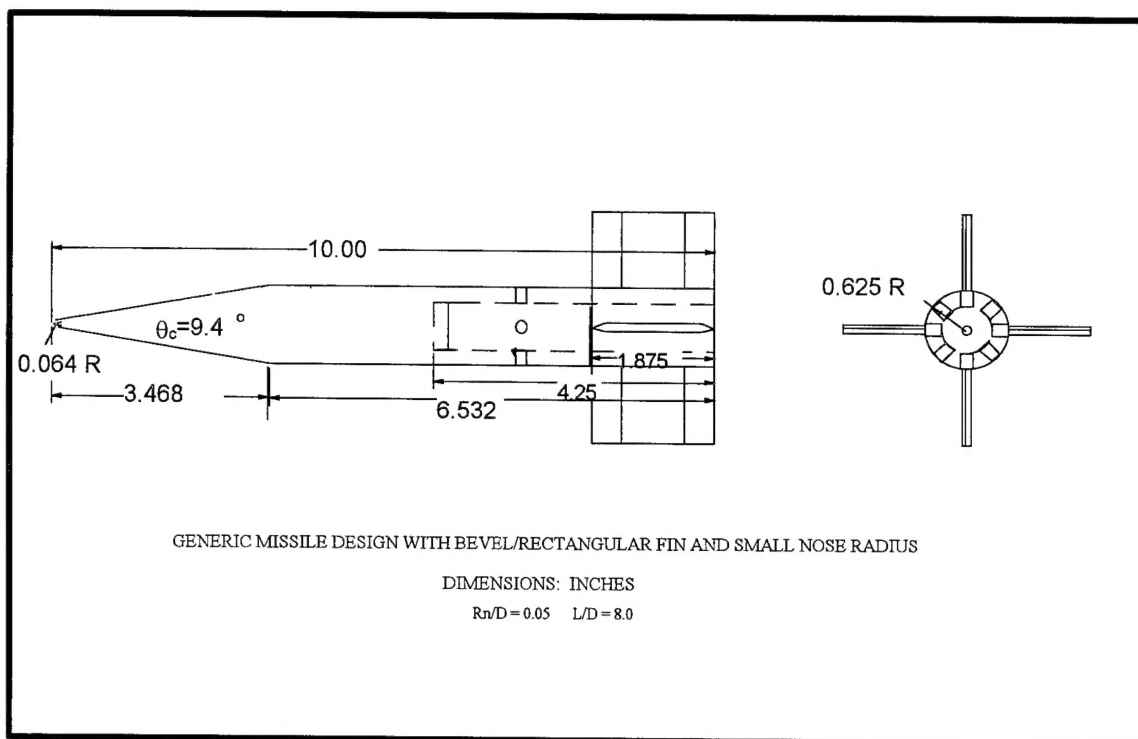


Figure 3: Two-view sketch of the generic missile model.

the nose for the heat-transfer model and at 3.468 in. (8.809 cm.) from the nose for the pressure model. For the forebody portion of the model, the diameter of the cylinder was 1.250 in. (3.175 cm.) and the overall length was 8.125 in. (20.638 cm.).

The fin section represented that portion of the missile from the fin leading edge to the fin trailing edge (which is also the base of the model). As noted earlier, the fin region (or afterbody) of the model used to obtain the forces and the moments was constructed of brass. Because the force-and-moment model was modular, it could be configured with one of two missile forebodies and one of two fin sections, providing for four different configurations. However, only the data obtained for the configuration with the small nose radius and the rectangular fins will be discussed in this paper. As shown in the sketch of Fig. 3, the rectangular fins had a root chord of 1.875 in. (4.763 cm.), with a tip-to-tip dimension (or span) of 3.75 in. (9.53 cm.), and an airfoil half angle (or deflection angle) for the leading and trailing edges of 9.7°.

The four fins were placed at a $\phi = 45^\circ, 135^\circ, 225^\circ$, and 315° , where ϕ is an angle measured relative to the leeward plane of symmetry. This is designated as an

“X” configuration in relation to the free-stream direction. Although care was always taken in positioning the model, the model could not be perfectly aligned with the tunnel centerline. The misalignment angle in the pitch plane (or α_{off}) was measured before and after almost every run. The offset angle of attack was added to the specified angle of attack to obtain the effective angle of attack for a given run.

$$\alpha_{\text{eff}} = \alpha_{\text{spec}} + \alpha_{\text{off}} \quad (2)$$

Comments Regarding Uncertainty and Repeatability

The experimental pressures are usually presented as the pressure measurement for a particular orifice (p) divided by the calculated value of the free-stream static pressure (p_1), yielding the dimensionless pressure parameter p/p_1 . A typical value of the pressure measured at the orifice located on the conical surface at zero angle of attack is 1.643 psia ($1.133 \times 10^4 \text{ N/m}^2$). Let us assume that the free-stream Mach number is 4.28 and that the stilling chamber pressure (p_{t1}) is 200.0 psia ($1.379 \times 10^6 \text{ N/m}^2$). The corresponding value of p_1 is 0.9130 psia ($6.295 \times 10^3 \text{ N/m}^2$) and the nominal value for the dimensionless parameter for the pressure measurement is 1.80.

The measured pressure is determined as the sum of the differential pressure sensed by the Kulite pressure transducer located in the scani-valve and the atmospheric pressure given by the Heise digital pressure indicator:

$$p = \Delta p_{\text{Kulite}} + p_{\text{atm}}$$

For the present example, the differential pressure sensed by the Kulite transducer is -9.557 psig ($-6.589 \times 10^5 \text{ N/m}^2$, gage) $\pm 0.075 \text{ psig}$ (517.10 N/m^2 , gage) and the atmospheric pressure is 11.200 psia ($7.722 \times 10^4 \text{ N/m}^2$) $\pm 0.006 \text{ psia}$ (41.37 N/m^2). Combining the extremes of the uncertainties, the measured pressure could be as high as 1.724 psia ($11.887 \times 10^3 \text{ N/m}^2$) or as low as 1.562 psia ($10.770 \times 10^3 \text{ N/m}^2$). Thus, the measured pressure at this orifice (which is in a region of the model unaffected by viscous/inviscid interactions) is 1.643 psia ($11.328 \times 10^3 \text{ N/m}^2$) $\pm 4.9\%$ -5.0% .

Since the free-stream static pressure (p_1) is calculated using:

$$p_1 = \left(\frac{p_t}{p_{t1}} \right) p_{t1} = \left[\left(1 + \frac{\gamma - 1}{2} M_1^2 \right)^{\frac{\gamma}{\gamma - 1}} \right] p_{t1} \quad (3)$$

there are two sources of uncertainty: the uncertainty in the pressure ratio because the free-stream Mach number can be as low as 4.24 or as high as 4.32 and the uncertainty in the stagnation pressure measurement itself. Combining the extremes of the uncertainties, the calculated value of p_1 could be as high as 0.9655 psia ($6.657 \times 10^3 \text{ N/m}^2$) or as low as 0.8635 psia ($5.953 \times 10^3 \text{ N/m}^2$). Thus, the reference pressure is 0.9130 psia ($6.295 \times 10^3 \text{ N/m}^2$) $\pm 5.75\%$ -5.42% . Combining these results, for this hypothetical case, p/p_1 could be as low as 1.562 or as high as 1.724, which represents an uncertainty band of $\pm 11.1\%$ -10.1% about the nominal value of 1.80. However, if one neglects the uncertainty in the free-stream pressure due to the uncertainty in the free-stream Mach number, the uncertainty in p/p_1 is approximately $\pm 6\%$.

Numerical Analysis

Using the shock-capturing GASP v3 code², the steady-state flowfields for a finless missile (which otherwise has the dimensions of the configuration presented in Fig. 3) at 0° , 10° , and 20° angles of attack were computed using the thin-layer Navier-Stokes (TLNS) equations in the nose region, i. e., the first 0.6% of the model, and the parabolized Navier Stokes (PNS)

equations aft of the nose region. GASP v3 offers numerous solution options to the user. The inviscid flux vectors were computed to second-order accuracy using van Leer's flux-vector splitting algorithm combined with the van Albada limiter to maintain stability and eliminate numerical oscillations in regions containing large gradients. The two-factor approximate factorization time-integration scheme was used to solve both the TLNS equations and the PNS equations. Solutions for the nose-region flowfield were considered converged, when the residual had decreased by two orders of magnitude. For the region where the PNS equations were used, solutions were considered converged, when the residual had decreased by three orders of magnitude. Free-stream flow conditions were specified at the inflow and at the farfield boundaries upstream of the bow shock wave. A second-order extrapolation boundary condition was specified for the downstream, out-flow boundaries. Boundary conditions at the surface of the vehicle included a no-slip requirement for the velocity boundary condition and a thermal boundary condition. Since the surface temperature changes during a run, flowfield computations were made for a range of realistic thermal boundary conditions. At the start of a run, the model is at room temperature, which is approximately 540°R (300K). The model cooled during the run, approaching the recovery temperature for long-duration runs. Therefore, flowfield computations were made for two assumed thermal boundary conditions at the wall: (1) the wall temperature is uniform at approximately 540°R (300K) and (2) there is no heat transferred from the air, i. e., the adiabatic wall assumption. Observations of the liquid-crystal patterns recorded during the present program indicated that boundary-layer transition occurred roughly 0.1L from the nose of the model (for low angles of attack). Thus, to cover the range of possible boundary-layer characteristics, computations were made assuming both that the boundary layer is fully turbulent starting at $x = 0.1L$ and that the boundary layer remains laminar for the entire length of the model.

Discussion of Results

As noted by Bertin et al.¹⁴, the four types of data that can be used for code-validation/code-calibration exercises are:

- (1) global measurements, such as the overall force and moment coefficients,

- (2) measurements at the surface of the vehicle or of the model, such as the static pressure at the surface or the temperature of the surface,
- (3) flow-visualization techniques, and
- (4) measurements within the shock layer.

Only data of the first three types will be presented in this paper.

Global Measurements

The experimental values of the global aerodynamic parameters: C_N , C_M , x_{cp}/L , and C_A are presented as functions of the effective angle of attack in Fig. 4. The force-and-moment data were obtained for a Mach 4.28 stream of air for free-stream Reynolds numbers based on the model length (in millions) of 15.2, 13.6, and 9.94. In order to obtain data over an angle-of-attack range from -10° to $+20^\circ$, two different model-support stings were used. Data in the angle-of-attack range -10° to $+10^\circ$, which are represented by the open symbols of Fig. 4, were obtained with a straight sting. Data in the angle-of-attack range 0° to $+20^\circ$, which are represented by the filled symbols of Fig. 4, were obtained with a bent sting. The experimentally-determined values of the global aerodynamic parameters are compared with the corresponding values computed using the ATAP code over a range of angles of attack from -10° to $+20^\circ$.

The experimental values of the normal-force coefficient are independent of the free-stream Reynolds number and of which sting was used (see Fig. 4a). The normal-force coefficients are a linear function of the angle of attack from -6° to $+6^\circ$. The agreement between the experimental values of C_N and the values computed using the ATAP code is considered reasonable, with the differences increasing as the angle of attack increases.

The experimental values of the pitching-moment coefficient, as referenced to the apex of the model, are presented in Fig. 4b. Again, the data are independent of the free-stream Reynolds number and of which sting was used. The experimentally-determined pitching-moment coefficients are in good agreement with the values computed using the ATAP code over the entire range of angles of attack tested.

Since the pitching moment is referenced to the apex of the model, the center of pressure was determined from the measurements using the approximation:

$$x_{cp} = M/N \quad (5)$$

The experimental and the ATAP-computed values of the nondimensionalized center-of-pressure location (x_{cp}/L) are in reasonable agreement (see Fig. 4c).

The axial-force coefficient is presented as a function of the effective angle of attack in Fig. 4d. For alphas greater than 18° , the axial-force-coefficient measurements exhibit a slight Reynolds-number dependence. This slight dependence isn't evident in the measurements below an alpha of 18° . However, the axial-force coefficients for other configurations tested in the overall program did not always exhibit a similar Reynolds-number dependence. Thus, this slight Reynolds-number dependence is an observation for limited, specific data and not a general conclusion.

Data obtained for the angle-of-attack range of 0° to $+10^\circ$ (the range of alpha overlap for the two stings) indicate that the axial-force coefficients for the straight sting (represented by the open symbols) were smaller than those measured when the model was supported by the bent sting (indicated by the filled symbols). Although the differences are consistent over this range of angle of attack, they are relatively small, about 5% or less.

There are several possible reasons for the differences between the experimental values of the axial-force coefficients and those computed using the ATAP code. The curved bow-shock wave can significantly affect the pressure distribution over the conical surface. Modeling the viscous/inviscid interaction between the boundary layer of the flow approaching the tail surfaces and the fin-induced shock wave, an interaction which is complicated by the three-dimensionality of the approach flow, which includes separated flow at the higher angles of attack. The base pressures measured for the low angle-of-attack runs when the model is mounted on the bent sting were much higher than those measured when the model was mounted on the straight sting. Since the bent sting represents an asymmetric obstruction to the wake flow, the authors believe that a viscous/inviscid interaction associated with the wake flow encountering the slanted portion of the bent sting propagated forward, influencing the flow in the base region. For angles of attack of 12° , or more, the bow shock wave intersected the fin-induced shock wave producing a complex shock/shock interaction.

Surface Measurements

In addition to comparing experimentally-determined values of global parameters, e. g., the force and the moment coefficients, with the corresponding values computed using the ATAP code, the experimentally-determined values of flow parameters at the surface of the model were compared with the corresponding values computed using the GASP v3 code. For the computation of the missile-body flowfields, a grid containing $121 \times 81 \times 65$ nodes in the ϵ -, η -, and ζ -coordinates, respectively, as illustrated in Fig. 5a, was created with a grid generation code. The far-field boundaries were placed far enough from the vehicle to capture the attached shock wave emanating from the nose of the missile. Points were clustered near the surface of the model, so that the distance to the first grid point off the surface is nominally $0.00036L$. Clustering also was used in the circumferential direction to provide greater detail of the flowfield near the plane of symmetry.

Measured values of the static pressure at the surface are presented in Fig. 6 for zero angle of attack. Referring to the locations presented in Table 1, the pressure orifices located on the conical surface alternate between the $\phi = 0^\circ$ and the $\phi = 180^\circ$ planes. Thus, the orifices are on opposite sides of the model. The nonzero values of the offset angle of attack, discussed previously, caused the effective angle of attack to be either 0.1° or 0.2° for these data. The fact that the model is actually at a slight angle of attack is believed to contribute to the "apparent" oscillatory nature of the pressures measured on the conical surface. Nevertheless, the experimentally-determined pressures are in reasonable agreement with the computed values for zero angle of attack. Included for comparison in Fig. 6 is the theoretical value of the pressure on a sharp cone having a conical half angle of 10° in a Mach 4.28 air stream, as calculated using the charts of NACA Report 1135 (Ref. 15). The agreement between the theoretical value of the sharp cone pressure, as calculated using the charts of Ref. 15, and the values for the pressure at the aft end of the conical frustum, as computed using GASP v3, is considered to be very good considering the differences between the actual flowfield and the flowfield for a sharp cone, which contains an attached, straight bow shock wave and which is the flow model for the Ref. 15 value.

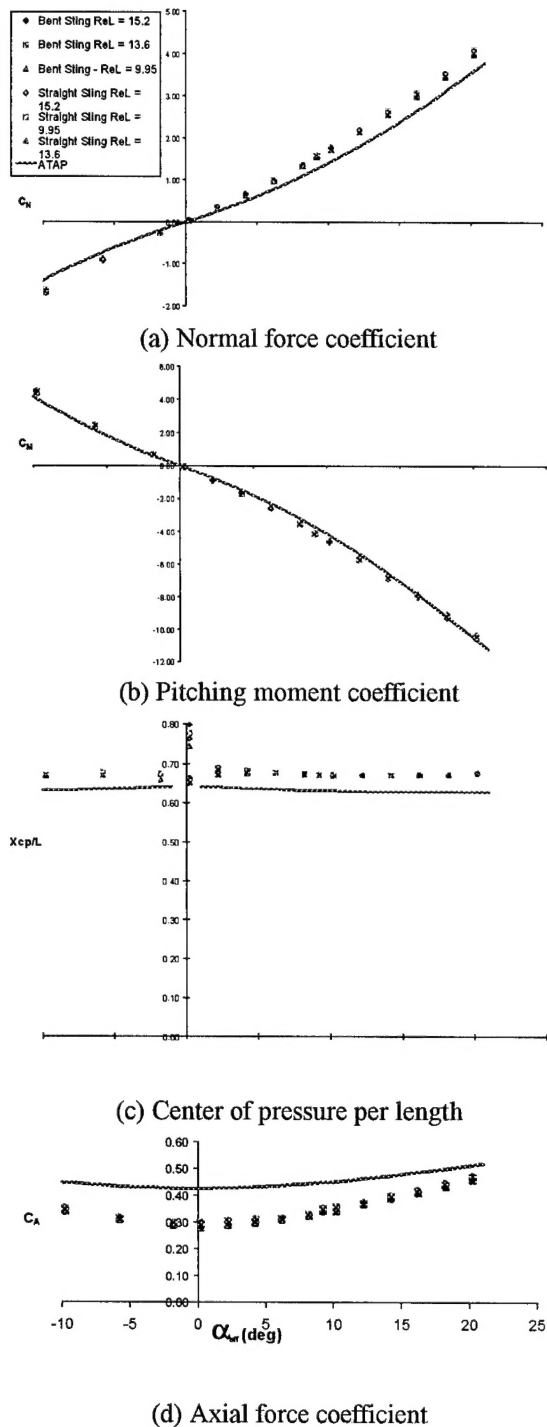
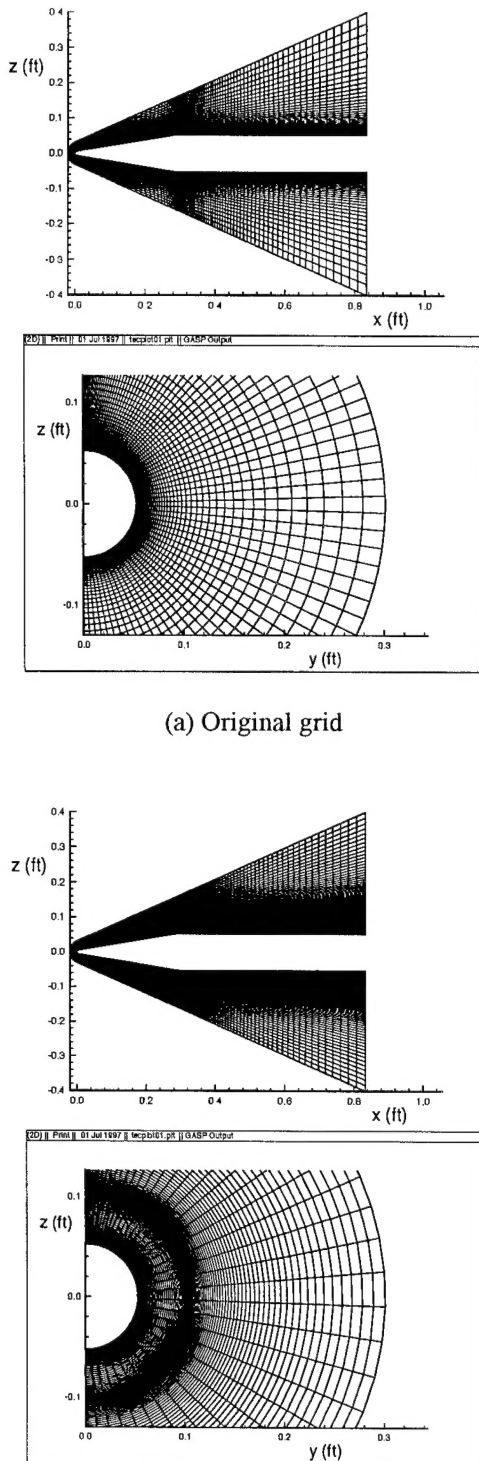


Figure 4: Experimentally-determined aerodynamic parameters as a function of the effective angle of attack for a generic missile in a Mach 4.28 air stream as compared with ATAP computations



(b) Modified grid, clustered for capturing the bow shock wave

Figure 5: Comparisons of grids used in GASP v3 pressure computations

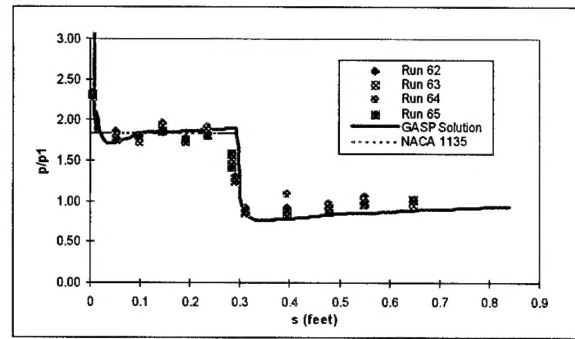


Figure 6: A comparisons of the measured surface pressure, GASP with those computed using GASP v3 and with Ref. 15 values for $\alpha = 0^\circ$, $ReL = 13.6$

Since aerothermodynamic data were obtained over an angle-of-attack range of -10° to $+20^\circ$, flowfields were computed for several nonzero angles of attack using the grid presented in Fig. 5a. The pressures thus computed when the model is at an angle of attack of 20° are presented in Fig. 7 (designated "laminar boundary layer, grid of Fig. 5a"). The pressures computed for the windward plane of symmetry exhibit an oscillatory variation in the streamwise direction at the end of the conical frustum and at the beginning of the cylindrical section. A detailed examination of the flowfield revealed a series of expansion waves and of compression waves reflecting across the shock layer, which would explain the computed pressure oscillations. Discussions with Oberkampf¹⁶ and Moore¹⁷ indicated that these pressure variations were probably anomalies associated with the computational algorithm. Green et al.¹⁸ reported benchmark flowfield computations by three different groups, noting that total-enthalpy fields produced by two codes that employed shock-capturing methods contained a small amount of numerical "noise", whereas shock-fit results exhibited no oscillations. The number of grid points in the normal direction for one of the shock capturing techniques was doubled as part of a grid-sensitivity exercise. Green et al.¹⁸ reported that "the level of grid sensitivity is believed to be small enough that grid resolution cannot be used to explain either the examples of agreement or disagreement between the results of the three groups." However, Oberkampf¹⁶ suggested that clustering points in the vicinity of the bow shock wave would improve the shock-capturing resolution and would, therefore, eliminate the anomalous pressure oscillations. Thus, a new grid was developed with $121 \times 41 \times 101$ points in the ϵ -, η -, and ζ -coordinates, respectively. As shown in Fig. 5b, the additional 36 points in the ζ -coordinate were clustered to correspond to the expected windward, mid-

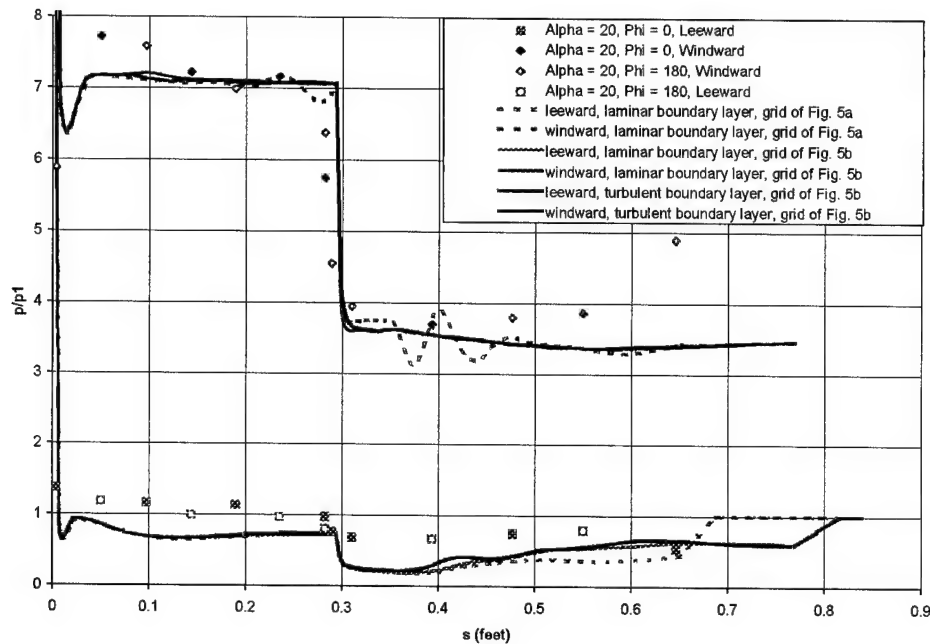
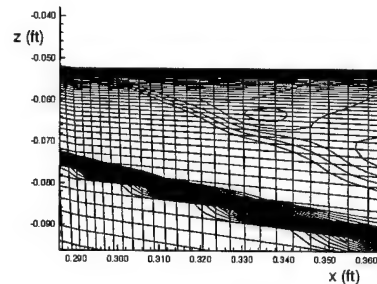


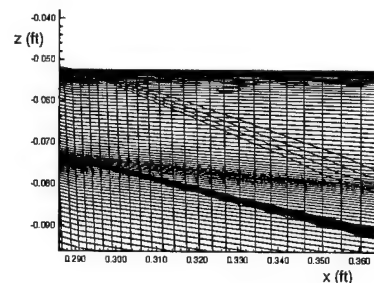
Figure 7: Comparisons of measured surface pressure distributions with those computed using GASP v3 illustrating the effect of the grid and of the boundary-layer character for $\alpha = 20^\circ$

cone location of the bow shock wave. As shown in the aft view of the grid (also Fig. 5b), the ζ -coordinate for the clustering was the same around the vehicle, i. e., was independent of the η -coordinate. Despite the relatively crude nature of the clustering strategy, the pressure distributions computed using the modified grid did not exhibit streamwise variations (see the computed pressure distribution designated "laminar boundary layer, grid of Fig. 5b"). The fact that the clustering strategy for the modified grid improved the resolution of the captured shock and eliminated the expansion waves and the compression waves reflecting across the shock layer is clearly evident in the iso-Mach-number contours presented in Fig. 8. For computations made with the original grid (see Fig. 8a), the captured shock wave is an extremely smeared structure. Furthermore, the iso-Mach number contours of Fig. 8a indicate the presence of left-running expansion waves impinging on the surface of the cylinder. For the computations made with the modified grid (see Fig. 8b), the shock wave is significantly less smeared. Furthermore, a right-running expansion fan can be seen, originating at the cone/cylinder interface, with the flow downstream of the corner being uniform.

Since the liquid crystal data indicated that boundary-layer transition occurred at an x/L of approximately 0.1, the flowfield was also computed with



(a) Computations for the original grid



(b) Computations for the modified grid, clustered for capturing the bow shock wave

Figure 8: Comparisons of iso-Mach contours for GASP v3 computed flowfields for $\alpha = 20^\circ$

the modified grid, but with the boundary-layer assumed to be turbulent downstream of $x = 0.1L$. The pressure distributions computed for a turbulent boundary layer are essentially the same as those computed for the laminar boundary layer using the same, modified grid (Fig. 5b).

A schlieren photograph with the model at an angle of attack of 20° is presented in Fig. 9a. Iso-Mach-number contours computed for the same angle of attack (and for the grid of Fig. 5b) are presented in Fig. 9b. The computed shock wave overlays perfectly onto the trace of the shock wave in the schlieren photograph.

Flow Visualization

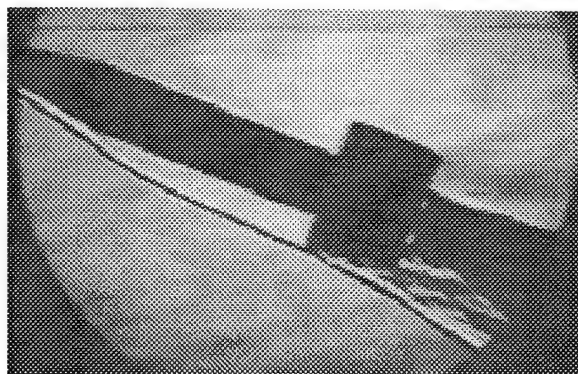
Coating the model with Thermochromic Liquid Crystals (TLCs) provided visual evidence of the surface temperature as a function of time and of location. As noted earlier, the color play for the TLCs used in the present tests indicates one particular temperature range, i. e., with a 0.9°F (0.5°C) bandwidth and a color play starting at 55.3°F (13.3°C) and ending at 54.4°F (12.8°C). The recovery temperature was calculated using¹³:

$$T_{\text{recovery}} = \left[r + \frac{1-r}{\left(1 + \frac{\gamma-1}{2} M_{\text{edge}}^2 \right)} \right] \quad (4)$$

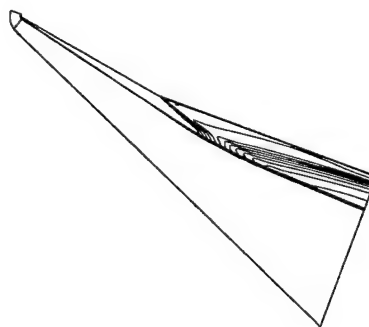
The calculated recovery temperature was 1.0°F (-17.2°C) assuming the boundary layer was laminar and was 26.1°F (-3.3°C) assuming the boundary layer was turbulent. At the start of a run, the model is at room temperature, approximately 80.0°F (26.7°C). Thus, the surface temperature for those regions of the model where the local heat-transfer coefficient is relatively large decreases rapidly toward the recovery temperature. In these regions, the TLC coating rapidly passes through the temperature range associated with its color play, leaving the model with a black appearance. In simple terms, the TLC coating will turn to black faster if the local heat-transfer coefficient is high, i. e., the cooling is relatively high. In regions where the local heat transfer coefficient is relatively low (such as would be the case in a separated flow region), the TLC coating remains blue. It is assumed that the wall temperature will eventually reach the recovery temperature, but over a very long time. Thus, it is assumed that the separation line is that line formed after 30 seconds of run time and will not move significantly over the allowable safe run

time of the tunnel (approximately 60 seconds). The separation line based on the TLC pattern for an angle of attack of 20° is highlighted in Fig. 10a. The highlighting is necessary due to the conversion from a color TIFF file to a black and white TIFF file. The distinct color band difference isn't apparent in the black and white format, thus it is highlighted for presentation in this paper.

To define the crossflow separation location at a given x-station based on the computed flowfield, the numerical solutions were examined to determine the ϕ



(a) Schlieren photograph



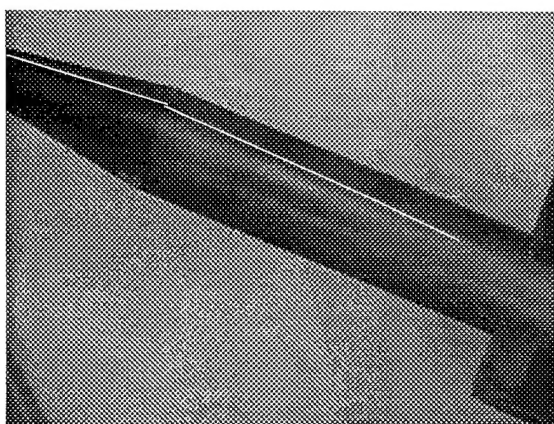
(b) Iso-Mach contours as computed using GASP v3

Figure 9: Comparisons of windward flowfield for the model at an $\alpha = 20^\circ$

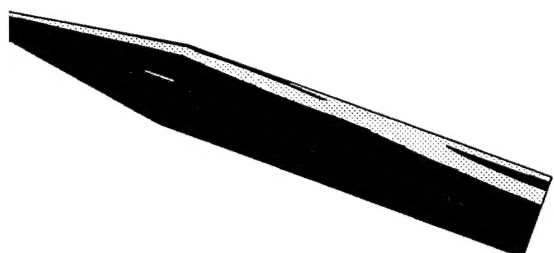
coordinate at which the circumferential velocity component changes sign. (Actually, it was at the first grid point off the surface that the flow was checked for the circumferential direction of the velocity.) The

change in sign of the circumferential component of velocity corresponds to the coalescence of streamlines from the attached crossflow on the windward side of the model and those of the recirculating, leeward, separated flow. These streamlines coalesce along the line representing the free-vortex separation from the model surface. The computational separation line thus determined from the sign change of the circumferential component of the velocity is presented in Fig. 10b.

As indicated in Fig. 10, the separation region as determined from the TLC pattern is in excellent agreement with that based on the GASP v3 computations for an angle of attack of 20° . There is also reasonable agreement between the separation region based on the TLC pattern and that based on the computed flowfield at an angle of attack of 10° , refer to Fig. 11.



(a) Separation line highlighted in TLC pattern



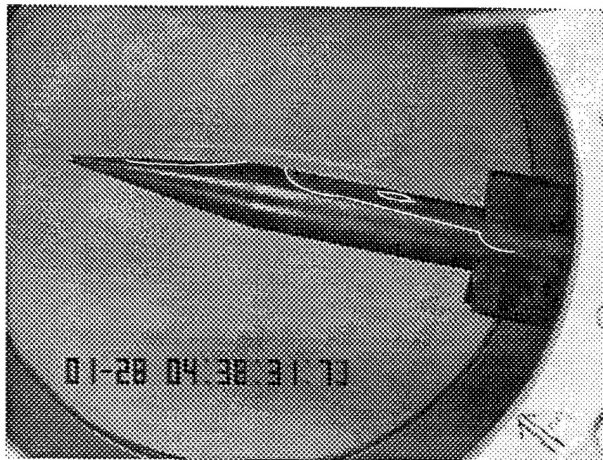
(b) GASP v3 separation region is light gray scaled, whereas the attached flow is black

Figure 10: Comparison of separation regions in a Mach 4.28 flowfield at $\alpha = 20^\circ$

At 10° angle of attack, reattachment lines can be seen in the TLC coating, see the highlighted lines in Fig. 11a. This is easily seen by the dark region of the main body of the missile. Thus, the black streaks prior to the fins in Fig. 11a indicates a region where the local heat-transfer coefficient is relatively high because of the recirculating flow reattaching to the surface. This black streak is also seen in the computational results, refer to Fig. 11b. However, there is a discrepancy between the computations and the TLC patterns in the vicinity of the interface between the conical frustum and the cylindrical section of the model. for an $\alpha = 10^\circ$. We will call the interface between the conical frustum of the model its shoulder. It is clear that there is a separation region on the conical section of the missile. The TLC pattern indicates a region after the "shoulder" of high heat transfer that is not indicated in the computations. The crystal also indicates from previous test runs the flow is transitional on the conical portion. This indicates the separated flow prior to the "shoulder" is in transition from laminar to turbulent. Due to the Prandtl-Meyer expansion at the "shoulder", the flowfield exhibits a more favorable pressure gradient and thus a fuller velocity profile. This fuller velocity profile causes the flowfield to increase the shear stresses at the surface thus increasing the heat transfer following the "shoulder". This would explain the liquid crystal indications at the "shoulder". This apparently is not the case when the angle of attack is 20° . The difference between the two cases would be a fully developed separation region on the conical section of the missile for an $\alpha = 20^\circ$ as opposed to a developing separation region at $\alpha = 10^\circ$. Therefore, analysis of the separation and reattachment region as a function of angle of attack can be determined.

The separation region circumferentially decreases in magnitude as the angle of attack increases. Thus, at $\alpha = 10^\circ$, the circumferential angle ϕ is averaged at approximately 40° , but at an $\alpha = 20^\circ$, the circumferential angle of the separation line decreases to an average value of approximately 30° . Computationally, the separation trend is not readily apparent. This maybe due to the laminar flowfield model used in GASP v3 computations. The separation line for both 10° and 20° can be readily seen on the conical section of both the computational and liquid crystal indications (refer to Figs. 11a and 11b). This indicates that separation for both angles of attack starts on the conical section of the generic missile configuration. The reattachment line also indicates a general trend associated with angle of attack.

As the angle of attack increases, it can be deduced that the reattachment line decreases in magnitude axially and decreases in circumferential angle from computational solutions. The relative distance between $\phi = 0^\circ$ and the separation line for $\alpha = 10^\circ$ and 20° maybe constant. This is difficult to determine since the only viewing angle possible is from the side plane or at a $\phi = 90^\circ$. For future modification to the USAFA Tri-Sonic Wind Tunnel, the priority will be to view the test models from the leeward surface. There is no supporting data which indicates Reynolds number sensitivity to reattachment or separation lines. The Reynolds number for these images were at $Re_L = 13.6$ million.



(a) Separation lines highlighted in TLC patterns



(b) GASP v3 separation region is light gray scaled, whereas the attached flow is black

Figure 11: Comparison of separation regions in a Mach 4.28 flowfield at $\alpha = 10^\circ$

Another point of interest is the fin interaction region. This region indicates a region of separation further downstream between the fins. This shock (from the rectangular fins) and boundary layer interaction caused the flow to separate. This was due to an adverse pressure gradient prior to the shock caused by the fins. This is easily seen when the effective angle of attack is zero as indicated in Fig. 12. This is consistent with the flowfield presented by Nishio¹⁹ for a fin attached to a flat plate. The data indicated a separation region prior to the shock wave generated by the fin's leading edge. This λ -like shock structure is consistent with the pattern in the TLC coating for $\alpha = 0^\circ$, which is presented in Fig. 12. This separation region is also present in the vicinity of the fins at other angles of attack.

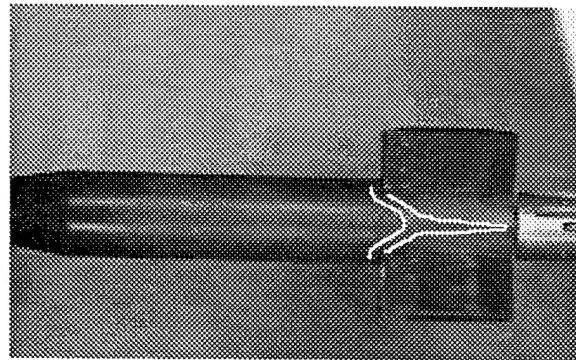


Figure 12: Separation regions in the fin areas due to the shock/boundary layer interaction a Mach 4.28 flowfield at $\alpha = 0^\circ$

Concluding Remarks

Based on the data obtained in the present program and on the comparisons of these data with parameters computed using the ATAP code and using the GASP v3 code, the following conclusions are made.

1. The experimentally-determined values of C_N , C_M , and x_{cp}/L were independent of the Reynolds number and of which sting was used to support the model in the wind tunnel. The engineering models used in the ATAP code provided suitable estimates of C_N , C_M , and x_{cp}/L .
2. There were significant differences between the experimentally-determined values of C_A and those computed using the ATAP code. The complex nature of the viscous/inviscid interactions involving the bow-

shock wave, the imbedded shock waves generated when the three-dimensional (sometimes separated) flow encounters the tail surfaces, and the base region flow contribute to these differences.

3. It was assumed that the validation of the models used in developing these codes is the responsibility of the code developer. However, in comparing the computed results to the experimental values, streamwise oscillations were observed in the computed pressure distribution on the windward surface of the missile at angle of attack. Detailed examination of the computed parameters revealed expansion waves and compression waves reflecting across the shock layer, consistent with the pressure distribution. However, discussions with experts on such flowfields and further computations of the flow revealed that the oscillating pressure distribution was anomalous, associated with the use of the shock-capturing technique. Simply doubling the number of grid points in the ζ direction did not significantly change the computed pressure distribution. The anomalous results could be eliminated by modifying the grid to cluster points for capturing the bow shock wave. As codes proliferate, more and more people are using the code, who have had nothing to do with the development of the code. It is important the codes are exercised for a wide variety of applications and the results documented, so that the user community can understand the possible sources of anomalies and their effect on the computed flowfields.

Acknowledgments

The authors appreciate the financial support provided by the Wright Laboratory/Armament Directorate/Munitions Seeker and Evaluation Branch (WL/FMGI) at the Eglin Air Force Base through Project Order QFY76219725005. Major Hubert G. Schneider and Tony Thompson of WL/FMGI served as Technical Officers for the effort. As one of the developers of the ATAP code, Jim Troler of Science Applications International Corporation (SAIC) also supported the authors of this paper.

The authors would like to thank the following people for their contributions to this effort: Capt. James E. Mayhew for computing thermodynamic properties associated with the tunnel flow, both Larry Lamblin, the tunnel technician, and Bobby Hatfield, the model builder, whose dedication and competence were critical to the successful execution of the test program

References

1. Gnoffo, P. A., Weilmuesnster, K. J., and Hamilton II, H. H., "Computational Aerothermodynamic Design Issues for Hypersonic Vehicles", AIAA 97-2473, 32nd Thermophysics Conference, Atlanta, GA, 1997.
2. Aerosoft, Inc., Blacksburg, VA 24060, "General Aerodynamic Simulation Program, version 3 (GASP v3), User's Manual, May 1996.
3. Bradley, R. G., "CFD Validation Philosophy", Paper No. 1, AGARD Symposium on Validation of Computational Fluid Dynamics, Lisbon, Portugal, May 1989.
4. Mehta, U. B., "Guide to Credible Computer Solutions of Fluid Flows", Journal of Propulsion and Power, Vol. 12, No. 5, Sep-Oct 1996, pp. 940-948.
5. Bradley, R. G., Private Transmittal, Jan. 1995.
6. Martellucci, A., "The Challenging Process of Validating CFD Codes", AIAA 90-1402, Seattle, WA, June 1990.
7. Dellinius, M. F. E., Lesieutre, D. J., Hegedus, M. C., Perkins, S. C., Jr., Love, J. F., and Lesieutre, T. O., "Engineering, Intermediate, and High Level Aerodynamic Prediction Methods and Applications", AIAA-97-2278, Atlanta, GA., June 1997.
8. Moore, F. G., "Current Status and Future Plans of the Aeroprediction Code", AIAA-97-2279, Atlanta, GA, June 1997.
9. Blake, W. B., "Missile DATCOM: 1997 Status and Future Plans", AIAA-97-2280, Atlanta, GA, June 1997.
10. Troler, J. W., Dougherty, C. M., Tincher, D. J., and Hall, D. W., "Wright Laboratory - Aerothermal Target Analysis Program (WL-ATAP Version 1.3 - February 1997), Volume 1: User's Guide", Science Applications International Corporation, Wayne, PA, Feb. 1997.
11. Ireland, P. T., Wang, Z., and Jones, T. V., "Liquid Crystal Heat Transfer Measurements", MEASUREMENT TECHNIQUES, Lecture Series 1995-01, von Karman Institute for Fluid Dynamics, Oxford University, United Kingdom.

12. Babinski, H., Edwards J. A., "Automatic liquid crystal thermography for transient heat transfer measurements in hypersonic flow", Experiments in Fluids, No. 21, pp. 227-236.
13. Bertin, J. J., Hypersonic Aerothermodynamics, AIAA Education Series, Washington, D. C., 1994.
14. Bertin, J. J., Martellucci, A., Neumann, R. D., and Stetson, K. F., "Developing a Data Base for the Calibration and Validation of Hypersonic CFD Codes - Sharp Cones", AIAA 93-3044, Orlando, FL, July 1993.
15. Ames Research Staff, "Equations, Tables, and Charts for Compressible Flow", Report 1135, NACA, 1953.
16. Oberkampf, W. L., "Private Communication", June 1997.
17. Moore, F. G., "Private Communication", June 1997.
18. Green, M. J., Lawrence, S. L., Dilley, A. D., Hawkins, R. W., Walker, M. A., and Oberkampf, W. L., "Application of CFD to a Generic Hypersonic Research Study", AIAA 93-0312, Reno, NV, Jan. 1993.
19. Nishio, M., "Visualization of Hypersonic Shock-Wave/Boundary Layer Interaction by Electric Discharge Method", AIAA 97-2288, 32nd Thermophysics Conference/15th Applied Aerodynamics, Atlanta, GA, 1997.